Available online at www.sciencedirect.com
ScienceDirect
Journal of Computational Physics 219 (2006) 104–119
JOURNAL OF COMPUTATIONAL PHYSICS
www.elsevier.com/locate/jcp

Two-dimensional computation of gas flow in a porous bed characterized by a porosity jump

D. Rochette [a,*], S. Clain [b]

[a] *Laboratoire Arc Electrique et Plasmas Thermiques, CNRS UMR 6069, Université Blaise Pascal, IUT de Montluçon, Avenue Aristide Briand, BP 2235, 03101 Montluçon Cedex, France*
[b] *Laboratoire de Mathématiques pour l'Industrie et la Physique, CNRS UMR 5640, Université Paul Sabatier Toulouse 3, 118 Route de Narbonne, 31062 Toulouse Cedex 4, France*

Received 15 December 2005; received in revised form 13 March 2006; accepted 17 March 2006
Available online 2 May 2006

Abstract

A finite volume method based on a VFRoe solver to simulate the flow of compressible gas in a variable porous medium for two-dimensional geometries is proposed. The modeling is based on the Euler system where a non-conservative term is added to take the porosity variation into account. A detailed presentation of the scheme is given, the main point is the construction of non-conservative fluxes to reproduce the non-conservation aspect of the problem. We compare the numerical method with an exact solution of the Riemann problem and we check that the method preserves steady-state situations even if we use a discontinuous jump for the porosity. Finally, we present two simulations involving a two-dimensional gas flow.

Keywords: Porosity jump; Finite volume; VFRoe solver; Non-conservative term

1. Introduction

In this paper, we present a numerical scheme for the unsteady two-dimensional Euler equations with a variable porosity. The homogenization process leads to a non-conservative hyperbolic system [17] and classical finite volume methods using a naive discretization of the non conservative term are not adequate since they do not preserve the stationary solution (see the example proposed in [16]). The model allows to simulate for example damping effects, gas flow cooled by a porous filter [14,19] where additional source terms would be introduced to characterize the porous medium – fluid interactions. Another class of problems motivated by industrial considerations is the simulation of a fast gas flow across grids. Since the obstacles are in most cases too small to be meshed, a homogenization approach is used with empirical laws to model the interactions between the grid and the flow.

Such a non-conservative hyperbolic problem is similar to the flow of compressible gas in a variable cross section duct model [4,5,10], where the cross section variation is considered as a discontinuous change in the

* Corresponding author. Tel.: +33 4 70 02 20 16; fax: +33 4 70 02 20 78.
E-mail address: rochette@moniut.univ-bpclermont.fr (D. Rochette).

0021-9991/$ - see front matter
doi:10.1016/j.jcp.2006.03.013

material porosity. The main difficulty is the non conservative term coming from the porosity or the cross section function. In [8], the authors give a mathematical sense to the non conservative term and several schemes, named well balanced schemes, have been proposed to solve correctly the non-conservative contribution [16,15]. In [20], a new scheme based on a VFRoe solver is presented, the method derives from the scheme established in [11] for the shallow water equation. All the above schemes have been developed for one-dimensional problems so we carry out in this article an extension for the two-dimensional case of the technique proposed in [20]. The method uses a VFRoe solver which consists into a local linearization of Riemann problems. Such a method is simpler to handle since we only deal with linear problems and avoid the complex exact resolution of the Riemann problem with porosity jump [3]. An other advantage is its ability to use complex gas law [6] but we do not consider this particular point in the present paper.

The paper is organized as follows. In Section 2, we describe the complete model of the system of governing equations. Section 3 is devoted to the numerical method based on a VFRoe scheme. In Section 4, we determine an exact solution to the Riemann problem in order to evaluate the behaviour of the numerical method. We also study the scheme convergence and the steady-state preservation using a comparison between the one-dimensional scheme, the two-dimensional scheme and the solution for stationary cases. Finally, in Section 5 we present two numerical simulations for test cases in two-dimensional problems.

2. Mathematical modeling

The two-dimensional governing equations for a gas flow in a variable porosity medium are based on the Euler equations [17,13,21]. Since the porosity is not constant, a non-conservative term appears in the impulsion equations during the homogenization process and the equations write:

$$\frac{\partial U}{\partial t}+\frac{\partial F(U)}{\partial x}+\frac{\partial G(U)}{\partial y}=\mathrm{NCT}(U), \tag{1}$$

with the notation

$$U=\begin{pmatrix}\phi\\ \rho\phi\\ \rho\phi u\\ \rho\phi v\\ \phi E\end{pmatrix},\quad F(U)=\begin{pmatrix}0\\ \rho\phi u\\ \rho\phi u^2+\phi P\\ \rho\phi uv\\ \phi u(E+P)\end{pmatrix}, \tag{2}$$

$$G(U)=\begin{pmatrix}0\\ \rho\phi v\\ \rho\phi uv\\ \rho\phi v^2+\phi P\\ \phi v(E+P)\end{pmatrix},\quad \mathrm{NCT}(U)=\begin{pmatrix}0\\ 0\\ P\partial\phi/\partial x\\ P\partial\phi/\partial y\\ 0\end{pmatrix}, \tag{3}$$

where ρ is the gas density, (u, v) is the velocity components, P is the pressure, ϕ is the variable porosity and E is the total energy per unit volume given by:

$$E=\rho\left(\frac{1}{2}V^2+e\right),$$

with e the specific internal energy and $V=\sqrt{u^2+v^2}$ the norm velocity field. In addition, to close the system, we use the ideal gas equation of state $P(\rho, e)=(\gamma-1)\rho e$ with $\gamma>1$, where γ denotes the ratio of specific heats. The gas is assumed to be ideal, so that:

$$e=C_{\mathrm{v}}T\quad\text{and}\quad S=C_{\mathrm{v}}\ln\left(\frac{P}{\rho^{\gamma}}\right), \tag{4}$$

where T is the gas temperature, C_{v} is the specific heat at constant volume and S is the entropy.

On the right-hand side, the non-conservative term $P\nabla\phi$ allows to take the porosity variation into account. Remark that the modeling is very similar to the variable cross section duct model where the cross section plays the same role than the porosity [4,5,10].

The system has to be completed with source terms to model the mechanical effects between the porous bed and the gas such as Darcy and Forchheimer laws and the convective heat transfer. In the sequel, we omit these terms which do not contain any derivative and therefore do not alter the hyperbolic structure of the equations. Moreover, they can easily be integrated using, for example, a splitting technique [19]. So, we only deal with the major difficulty i.e. the non-conservative term.

The VFRoe scheme is based on the resolution of Riemann problems at each side of the mesh. In order to define the generic Riemann problem, let us consider a line D passing to the origin separating the plan $\mathscr{P} = \mathbb{R}^2$ in two subdomains $\mathscr{P}_L$ and $\mathscr{P}_R$, we denote by $\boldsymbol{n}$ the normal vector to D going from $\mathscr{P}_L$ to $\mathscr{P}_R$ and $\boldsymbol{\tau}$ a normalised orthogonal vector to $\boldsymbol{n}$. In Fig. 1, vector (ξ, η) represents the new coordinate system in basis $(\boldsymbol{n}, \boldsymbol{\tau})$ where the coordinate ξ is the normal component and η is the tangential component.

For given left and right states U_L and U_R, the Riemann problem with initial condition $U = U_L$ in $\mathscr{P}_L$ and $U = U_R$ in $\mathscr{P}_R$ gives a solution invariant to translation following η. Therefore, using the change of variables to transform the coordinates (x, y) to the new ones (ξ, η) and exploiting the rotational invariance of the governing equations, we only deal with the flux $F(\widehat{U})$, where $\widehat{U}$ is the vector of the rotated conserved variables to solve Riemann problems [22].

In the rotated frame (ξ, η), the non-conservative expression of the system becomes an augmented one-dimensional system and the system reads:

$$\frac{\partial \widehat{U}}{\partial t} + A(\widehat{U})\frac{\partial \widehat{U}}{\partial \xi} = 0, \tag{5}$$

with $A(\widehat{U})$ the associated matrix:

$$A(\widehat{U}) = \begin{pmatrix} 0 & 0 & 0 & 0 & 0 \\ 0 & 0 & 1 & 0 & 0 \\ -P & -\hat{u}^2 + \frac{\gamma-1}{2}\widehat{V}^2 & (3-\gamma)\hat{u} & (1-\gamma)\hat{v} & \gamma - 1 \\ 0 & -\hat{u}\hat{v} & \hat{v} & \hat{u} & 0 \\ 0 & \hat{u}\left(\frac{\gamma-1}{2}\widehat{V}^2 - H\right) & H - (\gamma-1)\hat{u}^2 & (1-\gamma)\hat{u}\hat{v} & \gamma\hat{u} \end{pmatrix},$$

where $\hat{u}$ and $\hat{v}$ stand for the normal and tangential velocity, respectively, and the specific enthalpy H is defined by:

$$H = \frac{E+P}{\rho} = \frac{P}{\rho} + e + \frac{1}{2}\widehat{V}^2. \tag{6}$$

The matrix $A(\widehat{U})$ admits fives eigenvalues $\lambda_0 = 0$, $\lambda_1 = \hat{u} - c$, $\lambda_2 = \lambda_3 = \hat{u}$, $\lambda_4 = \hat{u} + c$ where c is the speed of sound given by:

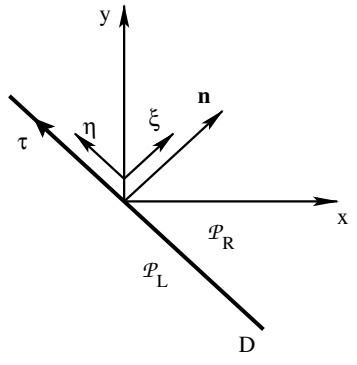

Fig. 1. New coordinate system for a general intercell boundary in two-dimensional domain.

$$c^2 = \frac{\gamma P}{\rho} = (\gamma - 1)\left(H - \frac{1}{2}\widehat{V}^2\right). \tag{7}$$

The corresponding right eigenvectors for linearly degenerate fields (λ_0, λ_2, λ_3) write:

$$R_0 = \begin{pmatrix} c^2 - \hat{u}^2 \\ \gamma P \\ 0 \\ \gamma P \hat{v} \\ P\left[H - \frac{(\gamma-1)}{2}\widehat{V}^2 + (\gamma-1)\hat{v}^2\right] \end{pmatrix}, \quad R_2 = \begin{pmatrix} 0 \\ 1 \\ \hat{u} \\ \hat{v} \\ \frac{1}{2}\widehat{V}^2 \end{pmatrix}, \quad R_3 = \begin{pmatrix} 0 \\ 0 \\ 0 \\ 1 \\ \hat{v} \end{pmatrix},$$

and the right eigenvectors for genuinely non-degenerate fields (λ_1, λ_4) are:

$$R_1 = \begin{pmatrix} 0 \\ 1 \\ \hat{u} - c \\ \hat{v} \\ H - \hat{u}c \end{pmatrix}, \quad R_4 = \begin{pmatrix} 0 \\ 1 \\ \hat{u} + c \\ \hat{v} \\ H + \hat{u}c \end{pmatrix}.$$

A critical situation occurs when λ_1 or λ_4 coincides with $\lambda_0 = 0$ leading to a parabolic degenerated system since the eigenvectors do not constitute a basis of $\mathbb{R}^5$ (see [3], Chapter 2). This particular situation induces numerical difficulties since we can not use the eigenvectors as a basis when $\hat{u} = c$ or $\hat{u} = -c$.

3. The numerical method

To deal with the numerical approximation, we introduce the following ingredients. $\mathscr{T}_h$ is a discretization of a two-dimensional polygonal bounded domain Ω with triangles S_i, $i = 1, \ldots, I$, where I is the number of mesh elements. For a given i, $v(i)$ represents the index set of the common edge elements $S_j \in \mathscr{T}_h$, $j \in v(i)$, where $L_{i,j} = \bar{S}_j \cap \bar{S}_i$ stands for the common side. In the sequel, $|L_{ij}|$ stands for the length of the side whereas $|S_i|$ is the area of the cell i. For a given side $L_{i,j}$, $\boldsymbol{n}_{i,j}$ represents the outwards normal of S_i pointing to S_j and $\boldsymbol{n}_{j,i} = -\boldsymbol{n}_{i,j}$. The sequence $(t^n)_n$ defines a time discretization of $[0, T]$ with $t^{n+1} = t^n + \Delta t$ and U_i^n stands for an approximation of the mean value of U at time t^n on the element S_i.

We consider a general finite volume scheme described in [22] in the context of the Euler equations:

$$U_i^{n+1} = U_i^n - \frac{\Delta t}{|S_i|}\sum_{j \in v(i)} |L_{i,j}| \mathscr{F}(U_i, U_j, \boldsymbol{n}_{i,j}), \tag{8}$$

where $\mathscr{F}$ is the numerical flux on the corresponding cell boundary in the rotated basis $(\boldsymbol{n}_{i,j}, \boldsymbol{\tau}_{i,j})$.

To solve numerically the non-conservative problem, we introduce a VFRoe method, initially proposed by [12,9] for the shallow water problem. The technique consists in a linearization of the Riemann problem at each interface $L_{i,j}$ using an intermediate state $\widetilde{W}$ to evaluate the matrix A. The particular point is that the numerical flux has to be non-conservative to take the term $P\nabla\phi$ into account i.e.

$$\mathscr{F}(U_i, U_j, \boldsymbol{n}_{i,j}) \neq \mathscr{F}(U_j, U_i, \boldsymbol{n}_{j,i}).$$

To this end, we consider the solution W of the new linearized problem:

$$\begin{aligned} &\tfrac{\partial W}{\partial t} + A(\widetilde{W})\tfrac{\partial W}{\partial \xi} = 0 \quad \text{for } (\xi, \eta) \in \mathbb{R}^2, \ t > 0, \\ &W(\xi, 0) = \begin{cases} \widehat{U}_{\mathrm{L}}, & \xi < 0, \ \eta \in \mathbb{R}, \\ \widehat{U}_{\mathrm{R}}, & \xi > 0, \ \eta \in \mathbb{R}, \end{cases} \end{aligned} \tag{9}$$

where $\widetilde{W} = \widetilde{W}(\widehat{U}_{\mathrm{L}}, \widehat{U}_{\mathrm{R}})$ is defined in the sequel.

In the conservative case, $\mathscr{F}$ is deduced from the intermediate state $W(0, t)$ taking $F(W(0, t))$ as numerical conservative flux. In the non-conservative case, we build the numerical flux from the conservative flux function

$\mathscr{F}$ and the intermediate states $W(0^-, t)$ and $W(0^+, t)$ situated on the left and on the right of the line $x = 0$. The non-conservative term does not explicitly appear in the flux expression but implicitly in the intermediate state evaluation [11].

Note that our method is different from the one proposed by [1,4] since the authors first discretize the conservative part of the operator and deduce a discretization of the non-conservative term using a steady-state constraint: a uniform constant pressure and velocity flow remains constant during its time evolution.

3.1. The VFRoe scheme

For a given average $\widetilde{W}$ defined from $\widehat{U}_{\mathrm{L}}$ and $\widehat{U}_{\mathrm{R}}$, the associated right eigenvectors $\widetilde{R}_k = R_k(\widetilde{W})$, $k = 0, \ldots, 4$ define a basis of $\mathbb{R}^5$ if $\tilde{u}^2 \neq \tilde{c}^2$ and we have the decomposition

$$\Delta W = \widehat{U}_{\mathrm{R}} - \widehat{U}_{\mathrm{L}} = \sum_{k=0}^{4} \widetilde{\alpha_k} \widetilde{R_k}. \tag{10}$$

Skipping the tilde for the sake of simplicity, coefficients α_k, $k = 0, \ldots, 4$ have to satisfy the following relations:

$$\Delta_0 = \phi_{\mathrm{R}} - \phi_{\mathrm{L}} = \alpha_0(c^2 - u^2), \tag{11}$$

$$\Delta_1 = (\rho\phi)_{\mathrm{R}} - (\rho\phi)_{\mathrm{L}} = \alpha_0\gamma P + \alpha_1 + \alpha_2 + \alpha_4, \tag{12}$$

$$\Delta_2 = (\rho\phi u)_{\mathrm{R}} - (\rho\phi u)_{\mathrm{L}} = \alpha_1(u - c) + \alpha_2 u + \alpha_4(u + c), \tag{13}$$

$$\Delta_3 = (\rho\phi v)_{\mathrm{R}} - (\rho\phi v)_{\mathrm{L}} = \alpha_0\gamma P v + \alpha_1 v + \alpha_2 v + \alpha_3 + \alpha_4 v, \tag{14}$$

$$\Delta_4 = (\phi E)_{\mathrm{R}} - (\phi E)_{\mathrm{L}} = \alpha_0\left[P\left(H - \frac{\gamma - 1}{2}V^2 + (\gamma - 1)v^2\right)\right] + \alpha_1(H - uc) + \alpha_2\frac{1}{2}V^2 + \alpha_3 v + \alpha_4(H + uc). \tag{15}$$

After calculation using Eqs. (14), (12) and (11), we obtain:

$$\alpha_0 = \frac{\Delta_0}{c^2 - u^2} \quad \text{and} \quad \alpha_3 = \Delta_3 - v\Delta_1. \tag{16}$$

Then one solves Eqs. (12), (13) and (15) to provide α_1, α_2 and α_4. Computationally, it is convenient to arrange the solution as follows:

$$\alpha_1 = \alpha_4 - \frac{1}{c}(\overline{\Delta}_2 - u\overline{\Delta}_1), \tag{17}$$

$$\alpha_2 = \overline{\Delta}_1 - \alpha_1 - \alpha_4, \tag{18}$$

$$\alpha_4 = \frac{1}{2}\left\{\frac{\gamma - 1}{c^2}\left[\overline{\Delta}_4 - u\overline{\Delta}_2 + \left(u^2 - \frac{1}{2}V^2\right)\overline{\Delta}_1\right] + \frac{1}{c}\left(\overline{\Delta}_2 - u\overline{\Delta}_1\right)\right\}, \tag{19}$$

where

$$\overline{\Delta}_1 = \Delta_1 - \alpha_0\gamma P = \alpha_1 + \alpha_2 + \alpha_4,$$

$$\overline{\Delta}_2 = \Delta_2 = \alpha_1(u - c) + \alpha_2 u + \alpha_4(u + c),$$

$$\overline{\Delta}_4 = \Delta_4 - \alpha_3 v - \alpha_0\left[P\left(H - \frac{\gamma - 1}{2}V^2 + (\gamma - 1)v^2\right)\right] = \alpha_1(H - uc) + \alpha_2\frac{1}{2}V^2 + \alpha_4(H + uc).$$

Note that the decomposition is not a priori defined when the gas velocity is sonic (i.e. $\tilde{u}^2 = \tilde{c}^2$) and $\Delta\phi \neq 0$. The five eigenvectors do not constitute a basis of $\mathbb{R}^5$ and the problem is no longer hyperbolic. Consequently, the proposed method is not adapted when a sonic point appears at point where the porosity changes. The exact solution $W = W_{i+1/2}(x/t; \widehat{U}_{\mathrm{L}}, \widehat{U}_{\mathrm{R}})$ of the linearized problem (9) is defined by [11]:

$$W((x/t)^-; \widehat{U}_{\mathrm{L}}, \widehat{U}_{\mathrm{R}}) = \widehat{U}_{\mathrm{L}} + \sum_{\frac{x}{t} > \tilde{\lambda}_j} \tilde{\alpha}_j \tilde{R}_j, \tag{20}$$

$$W((x/t)^+;\widehat{U}_L,\widehat{U}_R)=\widehat{U}_R-\sum_{\frac{x}{t}<\tilde{\lambda}_j}\tilde{\alpha}_j\tilde{R}_j. \tag{21}$$

Since $\lambda_0=0$ is an eigenvalue of $A(\widetilde{W})$, we consider two states on each side of $\xi=0$, depending on the other eigenvalues sign:

$$W(0^-;\widehat{U}_L,\widehat{U}_R)=\begin{cases}\widehat{U}_L & \text{if } \tilde{\lambda}_1>0,\\ \widehat{U}_L+\tilde{\alpha}_1\tilde{R}_1 & \text{if } \tilde{\lambda}_1<0<\tilde{\lambda}_2=\tilde{\lambda}_3,\\ \widehat{U}_R-\tilde{\alpha}_0\tilde{R}_0-\tilde{\alpha}_4\tilde{R}_4 & \text{if } \tilde{\lambda}_2=\tilde{\lambda}_3<0<\tilde{\lambda}_4,\\ \widehat{U}_R-\tilde{\alpha}_0\tilde{R}_0 & \text{if } \tilde{\lambda}_4<0\end{cases} \tag{22}$$

and

$$W(0^+;\widehat{U}_L,\widehat{U}_R)=W(0^-;\widehat{U}_L,\widehat{U}_R)+\tilde{\alpha}_0\tilde{R}_0. \tag{23}$$

When $\widehat{U}_L=\widehat{U}_i$ and $\widehat{U}_R=\widehat{U}_j$, the numerical flux function is given by:

$$\mathscr{F}(\widehat{U}_i,\widehat{U}_j,\boldsymbol{n}_{i,j})=F(W(0^-;\widehat{U}_i,\widehat{U}_j)).$$

It is important to note that $\mathscr{F}(\widehat{U}_i,\widehat{U}_j,\boldsymbol{n}_{i,j})\neq\mathscr{F}(\widehat{U}_j,\widehat{U}_i,\boldsymbol{n}_{j,i})$ since $W(0^+;\widehat{U}_i,\widehat{U}_j)\neq W(0^+;\widehat{U}_j,\widehat{U}_i)=W(0^-;\widehat{U}_i,\widehat{U}_j)$.

To get a complete numerical scheme, one has to set the local average $\widetilde{W}$. We propose the following expressions defined from four independent variables:

- $\widetilde{W}=\widetilde{W}(\widehat{U}_L,\widehat{U}_R)$ such that

$$\frac{1}{\tilde{\rho}}=\frac{1/\rho_L+1/\rho_R}{2},\quad \tilde{u}=\frac{\hat{u}_L+\hat{u}_R}{2},\quad \tilde{v}=\frac{\widehat{v}_L+\widehat{v}_R}{2},\quad \widetilde{P}=\frac{P_L+P_R}{2}. \tag{24}$$

Note that other variables are not obtained by averaging but are deduced from the primitive averaging values to satisfy the constitutive laws.

4. Numerical tests

4.1. Exact solution of the Riemann problem

The shock-tube in a porous medium described in Fig. 2 involves the gas flow in which the porosity is different in each part of the chamber.

The exact solution of the problem described in Fig. 2 for several choices of initial conditions was presented in [4,18]. Ref. [4] have shown that in some situations there is no uniqueness of the entropy solution to the Riemann problem. On the other hand, if the configuration of the wave curves is fixed, the entropy solution is unique, so here, we determine a solution to the Riemann problem, the left state is given and we fix the configuration of the wave curves.

4.1.1. First configuration

To compute the exact solution of the Riemann problem, we proceed as follows (see [3]): we prescribe a left state and choose the following configuration (see Fig. 3): 1-rarefaction wave, 0-stationary contact wave,

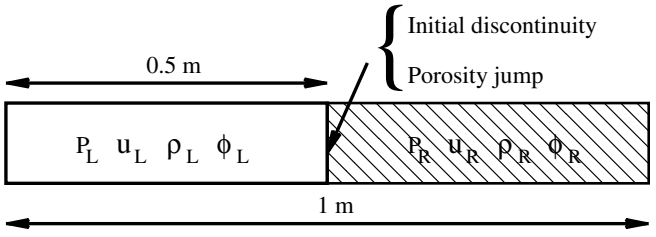

Fig. 2. Schematic description of the shock-tube in porous medium.

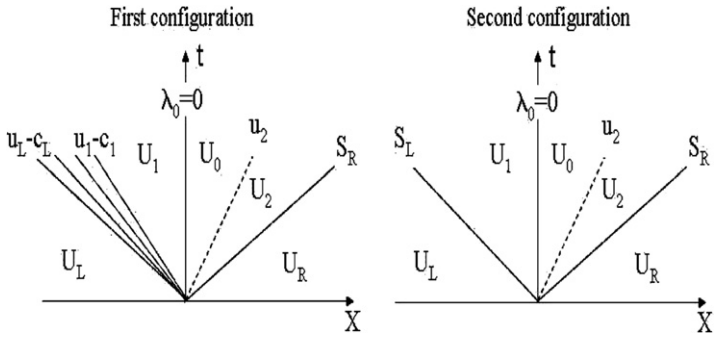

Fig. 3. Two configurations of wave curves of the Riemann problem with a porosity jump located at $x = 0$.

2-contact discontinuity wave, 3-shock wave. We deduce the other states using the Riemann invariants and the Rankine–Hugoniot conditions. For the first configuration, we take $P_L = 4 \times 10^5$ Pa, $\rho_L = 4.0$ kg m^{-3}, $u_L = 0.0$ m s^{-1} and $\phi_L = 1.0$. We compute the state U_1 using the Riemann invariants since we impose a rarefaction wave prescribing $u_1 = 80.0$ m s^{-1}. We then deduce P_1, ρ_1 and c_1. To evaluate the transition across the porous discontinuity, we use the Riemann invariants corresponding to the eigenvalue $\lambda_0 = 0$ i.e.:

$$\phi \rho u = \text{const.}, \tag{25}$$

$$S_i = \frac{P}{\rho^\gamma} = \text{const.}, \tag{26}$$

$$\frac{u^2}{2} + \frac{c^2}{\gamma - 1} = \text{const.}, \tag{27}$$

where S_i is the isentrope. Prescribing $\phi_R = 0.4$, we evaluate the other components of the state U_0 using a Newton algorithm to solve numerically Eqs. (25)–(27). To compute the state U_2, we use the Riemann invariants $u_2 = u_0$ and $P_2 = P_0$ and we impose $\rho_2 = 1.0725\rho_0$. At last, we compute the right state using the Rankine–Hugoniot conditions choosing $P_R = 0.3546\ P_2$. Table 1 sums up all the states.

In order to validate the two-dimensional model, we consider a rectangular domain $[0,1] \times [0,0.1]$ discretized with a unstructured mesh of 51,985 elements. Computations have been performed using the finite volume library developed by [23]. The initial conditions of the 2D simulation are the left state U_L and the right state U_R situated on each side of the initial discontinuity located at $x = 0.5$ m. Moreover, we let $v_L = 0$ m s^{-1} and $v_R = 0$ m s^{-1} to obtain a pure one-dimensional problem.

Fig. 4 represents the numerical results of density, pressure, x-velocity and entropy distributions and the exact solution to the Riemann problem. The solutions correctly predict the jump condition at $x = 0.5$ m and are in good agreement with the exact solution since they preserve a constant entropy across the porosity jump. Note that the contact discontinuity is extensively smeared, which is typical for a first-order scheme.

4.1.2. Second configuration

To compute the Riemann problem solution, we proceed in the same way. We choose the left state U_L with $P_L = 1 \times 10^5$ Pa, $\rho_L = 4.2$ kg m^{-3}, $u_L = 200.0$ m s^{-1} and $\phi_L = 1.0$. We use the second configuration described in Fig. 3: 1-shock wave, 0-stationary wave, 2-contact discontinuity wave, 3-shock wave. We list in Table 2 the intermediate states.

Table 1
Data for the first Riemann problem

	ϕ	ρ (kg m^{-3})	u (m s^{-1})	c (m s^{-1})	P (Pa)
U_L	1.0	4.0	0.0	374.16	4.0^5
U_1	1.0	3.21	80.0	358.16	2.95×10^5
U_0	0.4	2.54	253.11	341.69	2.12×10^5
U_2	0.4	2.72	253.11	329.94	2.12×10^5
U_R	0.4	1.34	25.56	280.05	7.5×10^4

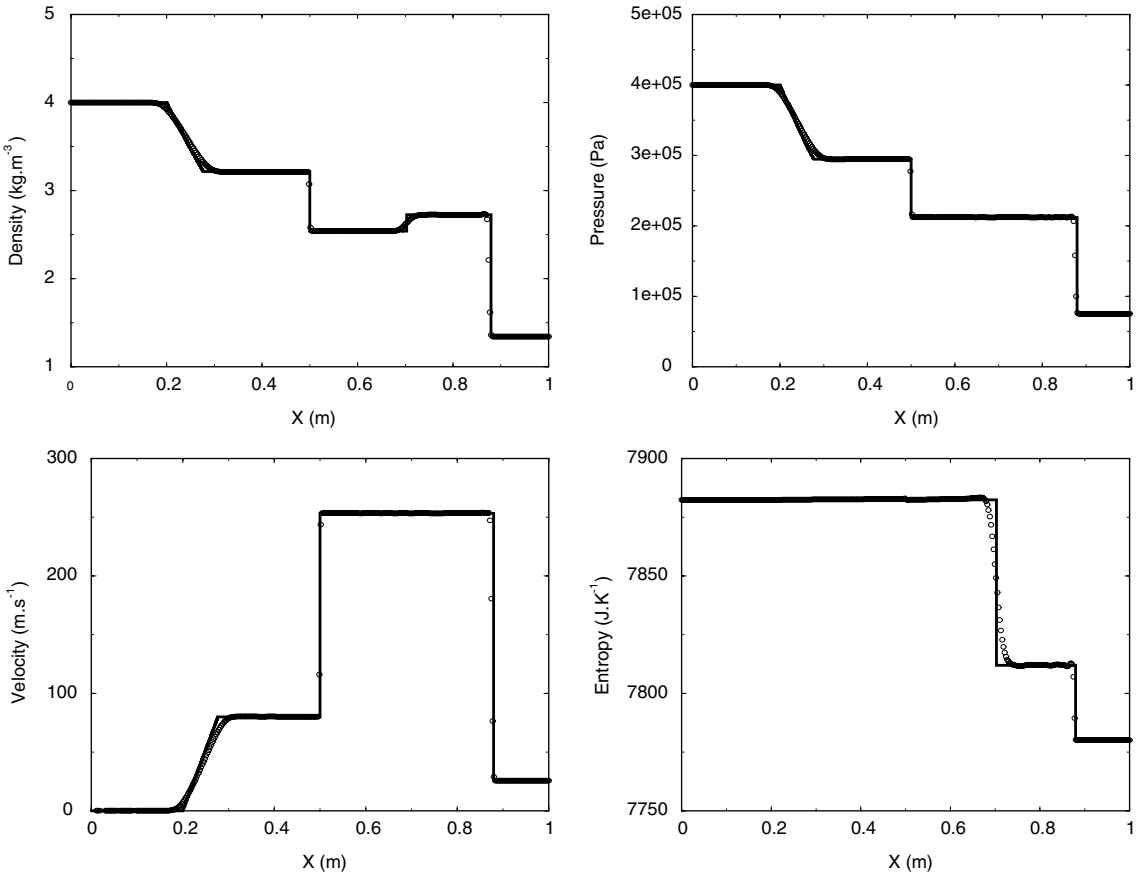

Fig. 4. Exact solution (solid line) and numerical results for the VFRoe scheme (symbol ○) at time $t = 8.02 \times 10^{-4}$ s.

Table 2
Data for the second Riemann problem

	ϕ	ρ (kg m^{-3})	u (m s^{-1})	c (m s^{-1})	P (Pa)
U_L	1.0	4.2	200.0	182.57	1×10^5
U_1	1.0	8.87	41.69	217.64	3.0×10^5
U_0	0.4	7.74	119.36	211.82	2.48×10^5
U_2	0.4	6.19	119.36	236.82	2.48×10^5
U_R	0.4	1.62	−199.07	146.22	2.48×10^4

Fig. 5 compares the exact solution and the numerical results obtained by the VFRoe scheme. In this configuration, the numerical results suit well with the exact solution. However, we observe small oscillations in the vicinity of the 1-shock and of the 3-shock which are transported during the simulation.

4.2. Convergence tests

To check the convergence of the numerical scheme, we perform a shock tube simulation in porous medium using several spatial cell sizes and compare the different numerical solutions with the exact solution defined in Section 4.1.1. To this end, we consider the above two-dimensional spatial domain and the initial conditions are analogous to Section 4.1.1. The mesh characteristics are given in Table 3 where h is the average space step and $h_{\min}$ the minimum space step used in the computation of the time step restricted by the CFL condition $\Delta t_{\max}|\lambda_i| \leqslant h_{\min}$.

Fig. 6 presents the density function in the x-direction for the exact solution and the numerical results for the four meshes. We observe a good convergence of the numerical solutions to the exact solution.

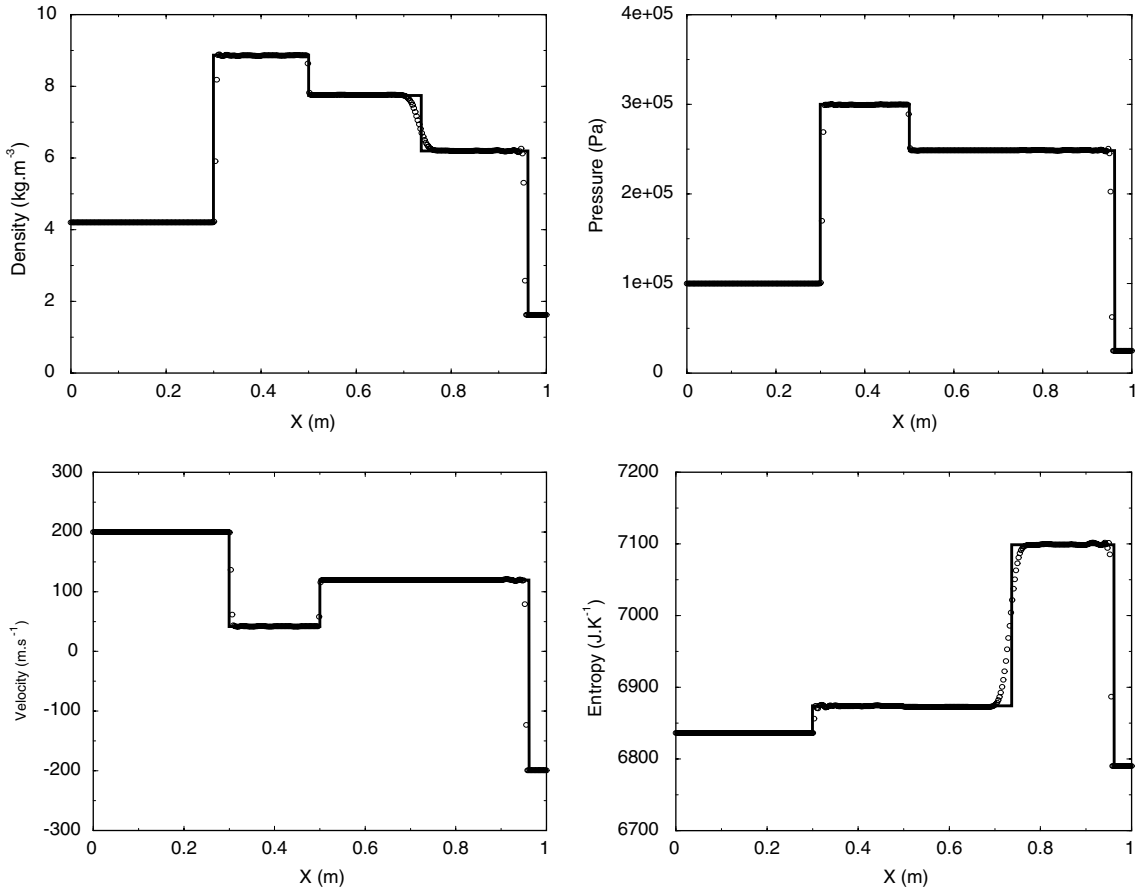

Fig. 5. Exact solution (solid line) and numerical results for the VFRoe scheme (symbol ∘) at time $t = 1.984 \times 10^{-3}$ s.

Table 3
Mesh characteristics for a $[0,1]\times[0,0.1]$ domain

Mesh	h (m)	$h_{\min}$ (m)	Cell numbers
1	1×10^{-2}	6.98×10^{-3}	2119
2	5×10^{-3}	3.34×10^{-3}	8195
3	2.5×10^{-3}	1.62×10^{-3}	33,025
4	1.25×10^{-3}	8.20×10^{-4}	132,843

4.3. Stationary solution

One of the major challenges for non-conservative hyperbolic problems is to produce numerical schemes able to maintain the stationary solution [1]. For a one-dimensional geometry, we have established in [20] that the stationary case with regular porosity (named the stationary model) reduces to ordinary differential equations:

$$\begin{aligned} &\rho\phi u = D_1, \\ &\frac{\gamma}{(\gamma-1)}P\phi u + \frac{1}{2}D_1u^2 = D_2, \\ &\frac{\mathrm{d}u}{\mathrm{d}x} = \frac{\gamma P u}{D_1 u - \gamma\phi P}\frac{\mathrm{d}\phi}{\mathrm{d}x}, \end{aligned} \tag{28}$$

where D_1 represents the constant mass flow rate and D_2 is a constant.

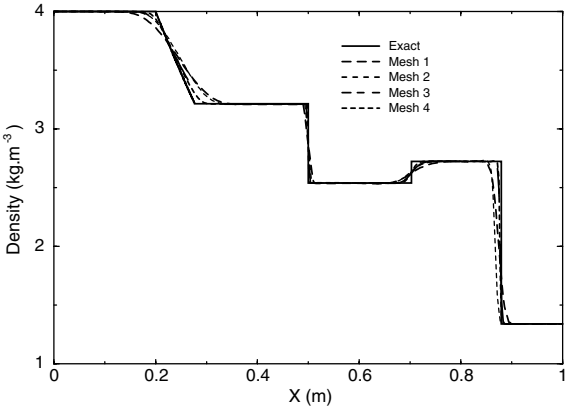

Fig. 6. Density distributions for the four meshes and the exact solution of the first configuration.

Furthermore, for a given inlet Dirichlet condition at point $x = 0$, we get a numerical approximation of the stationary problem solution on the whole domain, providing, in particular, the outlet condition at $x = 1$. We then assume that any theoretical non-stationary solution with the same inlet and outlet boundary conditions converges asymptotically to the stationary solution whatever the initial condition is. For the two-dimensional situation, we choose the initial condition and the boundary conditions such that $v = 0$ and then the problem turns into a one-dimensional problem following $(0x)$. We state homogeneous Neumann condition for the upper and lower boundaries ($y = 0$ and $y = 0.1$) and set inlet and outlet conditions at $x = 0$ and $x = 1$, respectively with $v = 0$ everywhere. The goal of this section is to compare the stationary solutions computed using the ordinary differential equation (28) and the VFRoe scheme for the one-dimensional problem as in [20] and the VFRoe scheme in two space dimensions.

4.3.1. Regular porosity function

In this example, we have chosen the continuous porosity function:

$$\phi(x) = \frac{2 + \sin(3\pi x)}{3}, \tag{29}$$

and we impose inlet boundary conditions $\rho_{\text{inlet}} = 3\ \text{kg m}^{-3}$, $P_{\text{inlet}} = 10^6\ \text{Pa}$, $v_{\text{inlet}} = 0\ \text{m s}^{-1}$ and $u_{\text{inlet}} = 100\ \text{m s}^{-1}$.

Fig. 7 shows the pressure and velocity distributions following the line $y = 0.05$ m of the solution computed with the VFRoe scheme. The curves correspond to the stationary solution obtained by solving the differential equation (28) using a fourth order Runge–Kutta method.

4.3.2. Discontinuous porosity function

We consider the situation where the porosity decreases abruptly from 1 to 0.3 at point $x = 0.5$ m for a steady state configuration. To test the numerical method, we smooth the discontinuity using a linear connection between $\phi = 1$ to $\phi = 0.3$ characterized by the interval length δ where the transition operates [16,7]. We study the behaviour of the numerical solution when δ becomes small (see Fig. 8). The extreme situation occurs when the transition takes place in only one element.

The stationary solution is obtained by imposing inlet boundary conditions $\rho_{\text{inlet}} = 3\ \text{kg m}^{-3}$, $P_{\text{inlet}} = 5 \times 10^5\ \text{Pa}$ and $u_{\text{inlet}} = 50\ \text{m s}^{-1}$ solving the ordinary differential Eq. (28) with a fourth order Runge–Kutta method on a 1000 regular cells mesh. With such a mesh, the regularization of the porosity occurs at least on 50 cells (passage of $\phi = 1$ to $\phi = 0.3$ with $\delta = 0.05$ m). We also compute the solution with the non-stationary problem using the 1D-model presented in [20] and the 2D-model. For the two-dimensional problem, we use a Delaunay regular mesh of 8195 cells such that the $h_{\min}$ parameter is greater than δ leading to a discontinuous transition from the numerical point of view. We also use the same boundary condition C_{inlet} on the left side and the condition $C_{\text{outlet}} = (\rho_{\text{outlet}}, u_{\text{outlet}}, P_{\text{outlet}})$ given by the stationary solution on the right side.

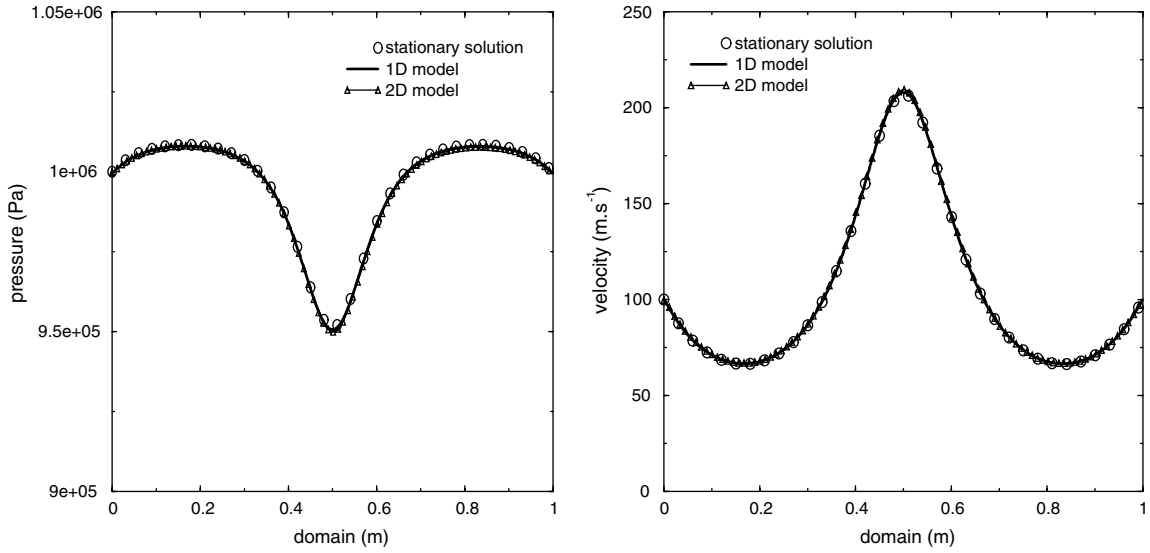

Fig. 7. Comparison of the pressure and velocity distributions between the stationary solution, numerical solutions obtained by the 1D and 2D models.

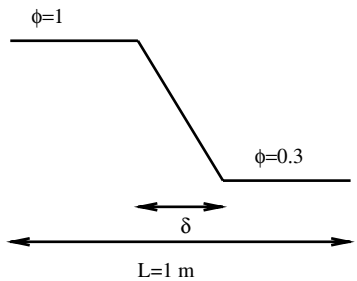

Fig. 8. Treatment of the porosity discontinuity with a regularized transition.

We impose symmetrical conditions for v on the top and bottom side to provide a solution invariant following (Oy).

We present in Fig. 9 the pressure and the velocity obtained by the analytic solution and the numerical solution for the 1D and 2D models. We observe a good agreement between the simulations and the stationary solution, we note for the 1D and 2D models a slight difference of the left and right pressures which decreases when the mesh is refined.

5. Two-dimensional numerical results and discussion

We present in this section two tests involving real two-dimensional problems in the $[0,1]\times[0,1]$ square geometry. The first test case is a two-dimensional simulation of a shock crossing a porous ball surrounded by air, this problem is analogous to the test case used in bifluid models presented in [2]. In the second example, we simulate a gas flow around a porous step (forward facing step), this test case is connected with the test case often called *Mach 3 wind tunnel with a step* (see [24]).

5.1. Shock/porous medium interaction

We consider a shock tube problem simulating the shock wave interaction with a spherical domain containing a porous medium. The shock travels from the left to the right of the domain at a constant speed before it hits the porous ball. In front of the shock, the porous ball of radius $r = 0.15$ m and center at $(x_0, y_0) =$

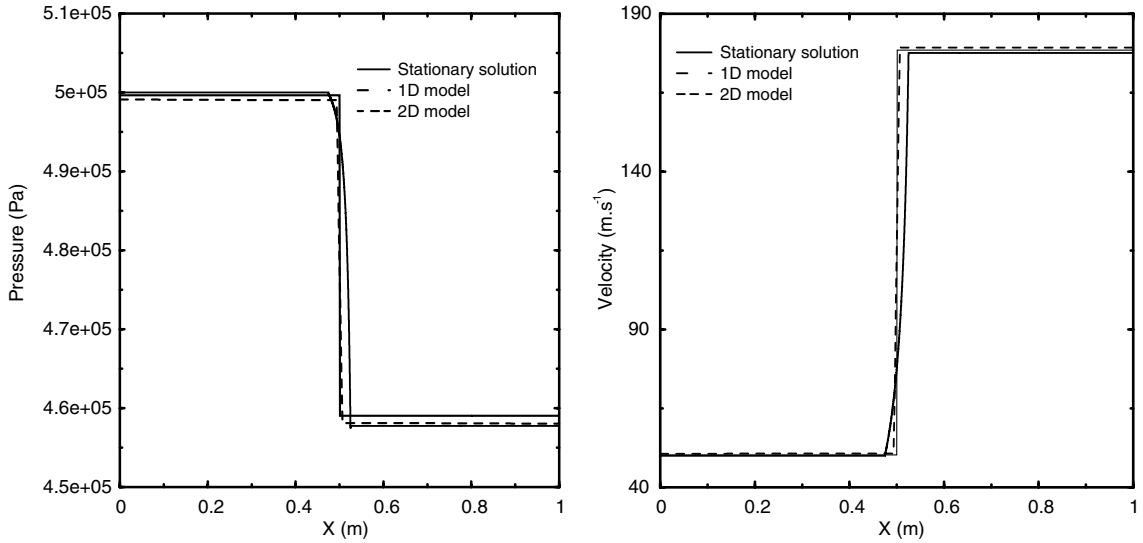

Fig. 9. Comparison of the pressure and velocity distributions between the stationary solution and numerical solutions obtained by the 1D and 2D models.

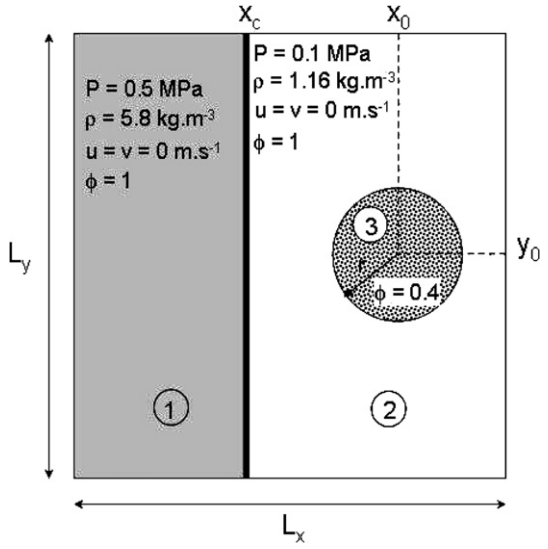

Fig. 10. Two-dimensional two-phase shock tube geometry with a porous ball.

(0.75, 0.5) is in equilibrium with the surrounding air (i.e. same pressure and same density, see Fig. 10). The domain is a $L_x = L_y = 1$ m square discretized with a unstructured mesh of 5098 cells.

A diaphragm is initially located at $x_c = 0.4$ m allowing to generate a shock wave, the initial conditions are summarized in Table 4.

Table 4
Initial state of the shock tube with a spherical porous medium

Location	ρ (kg m^{-3})	P (Pa)	$u = v$ (m s^{-1})	ϕ
Air ①	5.8	5×10^5	0	1.0
Air ②	1.16	1×10^5	0	1.0
Porous medium ③	1.16	1×10^5	0	0.4

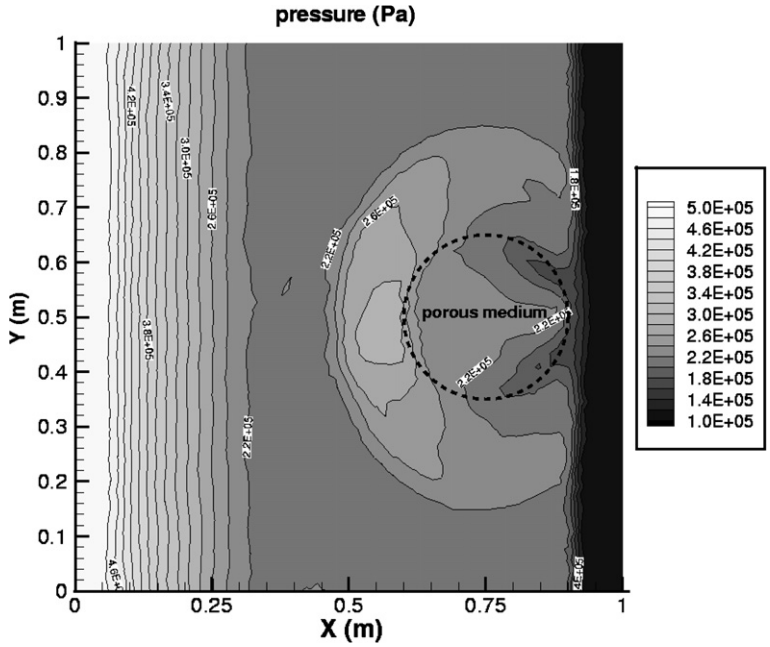

Fig. 11. Pressure contours at time $t = 1.2$ ms after the shock wave impact into a circular porous medium.

At the initial time the diaphragm rupture induces a shock wave which propagates toward the spherical porous medium. A part of the shock is transmitted to the porous medium where the gas flow velocity increases while a reflected wave goes back to the diaphragm. Readily in Fig. 11, circular pressure waves appear once the porous medium is reached by the shock. We observe a good symmetry of the numerical solution with respect to the line $y = 0.5$ m.

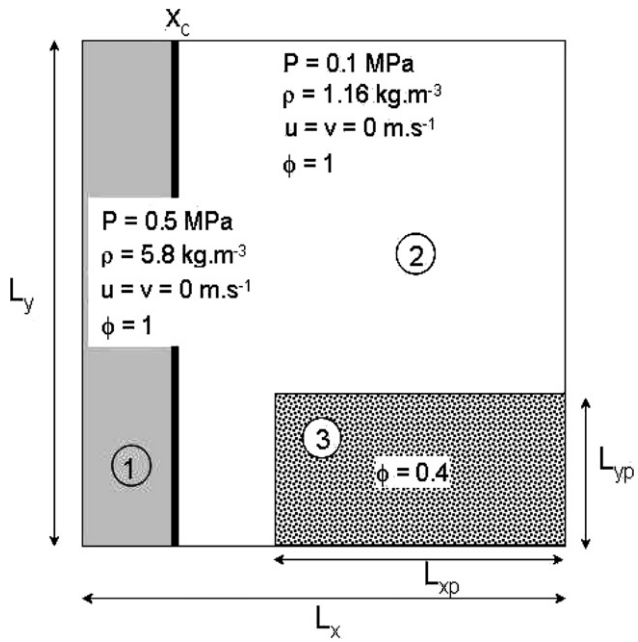

Fig. 12. Two-dimensional forward facing step geometry.

5.2. Forward facing step problem

In this simulation, we consider a shock wave crossing a porous step described in Fig. 12. We use a square domain with a 20,668 cells mesh for the discretization. A porous medium step of $L_{xp} = 0.6$ m length and $L_{yp} = 0.3$ m height is located at $[0.4, 1] \times [0, 0.3]$ surrounded by atmospheric air and the diaphragm is located at $x_c = 0.2$ m. The initial conditions are the same than the previous test.

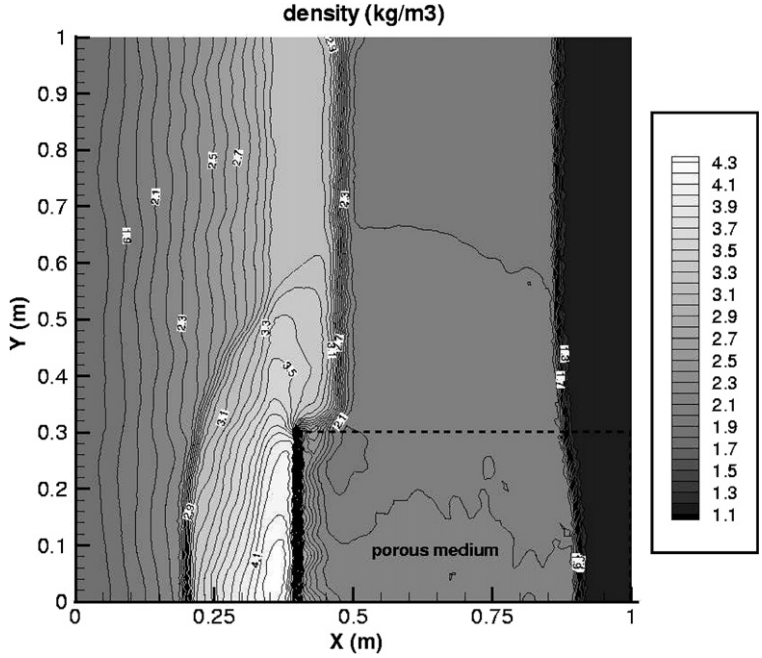

Fig. 13. Density contours for the forward facing step problem at time $t = 1.4$ ms.

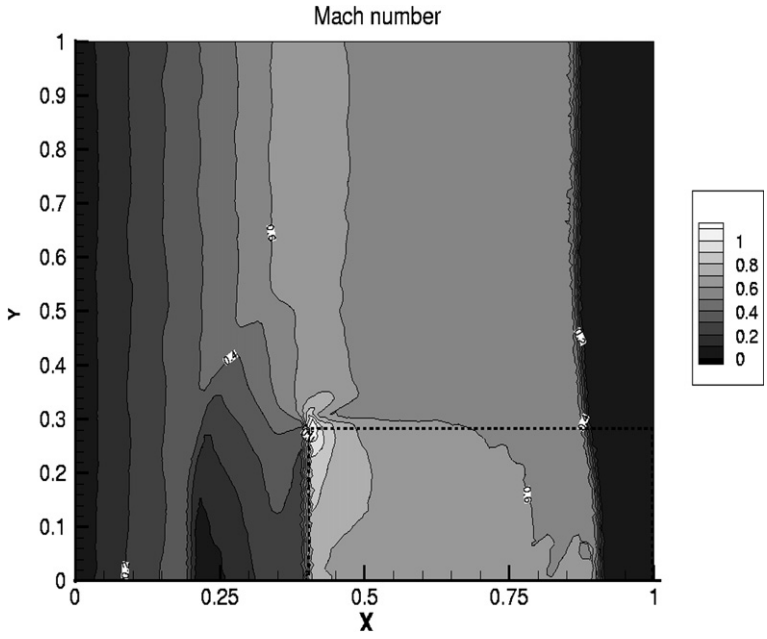

Fig. 14. Mach number contours for the forward facing step problem at time $t = 1.5$ ms.

Fig. 13 shows the density isovalues for the forward facing step problem. In the upper part, we clearly distinguish from right to left the shock wave, the contact discontinuity and the rarefaction wave. In the lower part, a more complex situation takes place front of the porous medium where the gas is compressed. We note that the transmitted wave is slightly faster in the porous medium than in air and the reflected wave is clearly visible.

Fig. 14 shows the Mach number isovalues. The higher gas velocity is located at the step corner where the gas velocity is close to the sound velocity inside the porous medium. This test reaches the limits of the numerical method because at the porosity jump: a 1-rarefaction wave is generated and the last 1-characteristic speed is close to zero ($u \approx c$), i.e. the 1-rarefaction wave touches the stationary contact from the right leading to a parabolic degeneracy.

6. Conclusion

We have proposed a first order two-dimensional finite volume scheme for compressible flow in variable porosity medium. The flux approximation is based on a VFRoe solver allowing to consider more complex constitutive laws for the gas. Exact solutions have been directly compared with solutions generated by the non-conservative numerical method and we obtain a good agreement with the correct solution. Numerical experiments show that the scheme preserves the steady-state even if a porosity discontinuity occurs. Numerical simulations for more complex situations have also been presented to experiment the numerical scheme with real two-dimensional problems. The main point is that the scheme manages to handle discontinuous porosity function which is of practical interest like the porous filter [19]. The negative point is that the scheme can not hold sonic situations where the porosity changes since the eigenvector basis degenerates.

Acknowledgements

The authors thank F. Gentils and J. Wild of Schneider Electric for their financial support.

References

[1] R. Abgrall, R. Saurel, A multiphase Godunov method for compressible multifluid and multiphase flows, Journal of Computational Physics 150 (1999) 425–467.
[2] G. Allaire, S. Clerc, S. Kokh, A five-equation model for the simulation of interfaces between compressible fluids, Journal of Computational Physics 181 (2002) 577–616.
[3] N. Andrianov, Analytical and numerical investigation of two-phase flow, PhD Dissertation, Fafakultät für Mathematik, Universität Magdeburg, 2003.
[4] N. Andrianov, G. Warnecke, On the solution to the Riemann problem for the compressible duct flow, SIAM Journal of Applied Mathematics 64 (3) (2004) 878–901.
[5] M. Barret, E. Faucher, J.M. Hérard, Schemes to compute unsteady flashing flows, AIAA Journal 40 (5) (2002) 905–913.
[6] T. Buffard, T. Gallouët, J.M. Hérard, A sequel to a rough Godunov scheme: application to real gases, Computers and Fluids 29 (2000) 813–847.
[7] A. Chinnayya, A.Y. LeRoux, N. Seguin, A well-balanced numerical scheme for shallow-water equations with topography: resonance phenomena, International Journal on Finite Volumes (2004).
[8] G. Dal Maso, P.G. Le Floch, F. Murat, Definition and weak stability of a non-conservative product, Journal de Mathematiques Pures et Appliquees 74 (1995) 483–548.
[9] I. Faille, T. Gallouët, J.M. Masella, On a approximate Godunov scheme, International Journal of Computational Fluid Dynamics 123 (1999) 133–149.
[10] E. Faucher, J.M. Hérard, M. Barret, C. Toulemonde, Computation of flashing flows in variable cross section ducts, International Journal of Computational Fluid Dynamics 13 (3) (2000) 365–391.
[11] T. Gallouët, J.M. Hérard, N. Seguin, Some approximate Godunov schemes to compute shallow-water equations with topography, Computers and Fluids 32 (2003) 479–513.
[12] T. Gallouët, J.-M. Masella, Un schéma de Godunov approché, Comptes Rendus de l Academie des Sciences Serie I-Mathematique, Paris 323 (2003) 77–84.
[13] T. Gallouët, R. Saurel, Modèles et méthodes numériques pour les écoulements fluides, cours de DEA, Centre de Mathématiques et d'Informatique, Université de Provence, 1998.
[14] F. Gentil, D. Serve, P. Chevallier, Un filtre innovant pour la protection contre les effets de l'arc interne dans les cellules moyenne tension, in: Proceedings of the Seconde Conférence Européenne sur les Matériels de Postes HT et MT (Matpost 03), Lyon, France, 2003.

[15] L. Gosse, A well-balanced scheme using non-conservative product designed for hyperbolic systems of conservative laws with source terms, M3AS 11 (2) (2001) 339–365.
[16] J.M. Greenberg, A.Y. Leroux, A well-balanced scheme for the numerical processing of source terms in hyperbolic equations, SIAM Journal of Numerical Analysis 33 (1) (1996) 1–16.
[17] M. Ishii, Thermo-fluid Dynamic Theory of Two-phase Flow, Eyrolles, Paris, 1975.
[18] C.A. Lowe, Two-phase shock-tube problems and numerical methods of solution, Journal of Computational Physics 204 (2005) 598–632.
[19] D. Rochette, S. Clain, Local heat transfer of compressible fluid in porous media: application to the HBC fuse, International Journal of Heat and Fluid flow 26 (2005) 322–333.
[20] D. Rochette, S. Clain, T. Buffard, Numerical scheme to compute a compressible gas flow in variable porosity media, International Journal of Computational Fluid Dynamics 1 (4) (2005) 299–309.
[21] R. Saurel, O. Lemetayer, A multiphase model for compressible flows with interfaces, shocks, detonation waves and cavitation, Journal of Fluid Mechanics 431 (2001) 239–271.
[22] E.F. Toro, Riemann Solvers and Numerical Methods for Fluid Dynamics, Springer-Verlag, Berlin, 1997.
[23] R. Touzani, Object Finite Element Library, Copyright ©1998–2003 Rachid Touzani. Available from: <http://ofeli.sourceforge.net/>.
[24] P. Woodward, P. Colella, The numerical simulation of two-dimensional fluid with strong shocks, Journal of Computational Physics 54 (1984) 115–173.